LA-UR-16-26012
Approved for public release; distribution is unlimited.

Title: L4 Milestone Report for MixEOS 2016 experiments and simulations

Author(s): Loomis, Eric Nicholas
Bradley, Paul Andrew
Merritt, Elizabeth Catherine
Guzik, Joyce Ann
Denne, Patrick Hagen

Intended for: Report

Issued: 2016-08-04

L4 Milestone Report for MixEOS 2016 experiments and simulations

Eric Loomis, Paul Bradley, Elizabeth Merritt, Joyce Guzik, and Patrick Denne

August 01, 2016 (Memo XCP-6:16-020)

Introduction

Accurate simulations of fluid and plasma flows require accurate thermodynamic properties of the fluids or plasmas. This thermodynamic information is represented by the equations of state of the materials. For pure materials, the equations of state may be represented by analytical models for idealized circumstances, or by tabular means, such as the Sesame tables. However, when a computational cell has a mixture of two or more fluids, the equations of state are not well understood, particularly under the circumstances of high energy densities. This is a particularly difficult issue for Eulerian codes, wherein mixed cells arise simply due to the advection process. LANL Eulerian codes typically assume an "Amagat's Law" (or Law of Partial Volumes) for the mixture in which the pressures and temperatures of fluids are at an equilibrium that is consistent with the fluids being segregated within the cell. However, for purposes of computing other EOS properties, e.g., bulk modulus, or sound speed, the fluids are considered to be fully "mixed". LANL has also been investigating implementing instead "Dalton's Law" in which the total pressure is considered to be the sum of the partial pressures within the cell. For ideal gases, these two laws give the same result. Other possibilities are non-pressure-temperature-equilibrated approaches in which the two fluids are not assumed to "mix" at all, and the EOS properties of the cell are computed from, say, volume-weighted averages of the individual fluid properties. The assumption of the EOS properties within a mixed cell can have a pronounced effect on the behavior of the cell, resulting in, for example, different shock speeds, pressures, temperatures and densities within the cell. There is no apparent consensus as to which approach is best under HED conditions, though we note that under typical atmospheric and near atmospheric conditions the differences may be slight.

Recent work by Kress and others using QMD techniques suggest that the EOS mixing rules are not so simple for fluids under HED conditions, and that significant errors can arise when they are applied to compute the bulk thermodynamic properties (pressure, temperature, density) of mixtures under HED conditions. See, for example, Maygar & Mattsson (Physics of Plasmas 20, 032701, 2013) for a discussion of mixing rule predictions compared to density-functional theory/QMD simulations

for a Xe-D mixture under HED conditions, showing that the QMD result lies between the Amagat and Dalton rule predictions. Unfortunately, the cost of these QMD calculations preclude using them to generate full thermodynamic tables for mixtures of interest, in order to assess the potential impact of these errors on code predictions. In addition, if two separate materials mix, there is a range of mix concentrations and this would require a large range of EOS tables corresponding to each mixture composition. Clearly, there needs to be an approximate way to combine EOS tables to create a mixture EOS.

We have conducted experiments at the OMEGA-EP laser facility (Univ. Rochester, NY) providing EOS data, in the form of shock speed, of atomic mixtures of Ni and Al. These experiments were successfully concluded following our second shot day in January 2016 where shock velocities in reference and standard materials (Al and quartz) were measured along with those in test specimens of NiAl compound. In the remainder of this report we discuss our design strategy, the experiments and data, and post shot calculations with inline mixture rules for the test specimens.

Design strategy and planning

Our top-level measurement strategy was based around the OMEGA-EP velocity interferometry system (VISAR) because this technique is known to produce highly accurate measurements of shock-driven hydrodynamics. This diagnostic is the workhorse for the field of experimental shock physics because of this accuracy. In order to obtain a full thermodynamic state (i.e., p, V, u_s, u_p) from a single shock measurement, at least two different parameters of that state must be measured since the Rankine-Hugoniot shock jump conditions will relate all other parameters to those two. When possible, the VISAR (or multiple VISARs) measure the shock speed and particle velocity (or free surface velocity) as the two free parameters; however, under laser-driven HED conditions this is extremely difficult for a variety of reasons. What is done instead is to use either shock transit time methods or utilize the property of transparent insulators where the shock front becomes reflecting above 1 Mbar (due to insulator-metal transition). Under this condition the VISAR then measures the shock speed directly. Simultaneous measurements of a 'standard' material where the EOS is known, is then required to determine the remaining state parameter of the test specimen.

In our experiments we placed a quartz standard next to our test (or reference) metal specimen all on top of a thick ablator material used to efficiently create high pressure 10's Mbar shocks. This target geometry is shown in Fig. 1. With the VISAR we measured the shock velocity inside the quartz standard as well as the shock transit time through our opaque metal test specimens. Since the EOS of quartz is well-known, measuring the shock speed is sufficient to give us its shock pressure, which we also used to infer the shock pressure inside the ablator whose EOS we also assumed known (polystyrene and beryllium). Once the ablator shock pressure was

known, along with any time dependent variations as measured inside the quartz, we could apply that pressure in our simulations for each mixture rule and see which gave the closest prediction to the measured shock transit time through the test specimen. As a further test of this technique we repeated the experiments on Al reference specimens, whose EOS is assumed known, to verify the strategy was sound.

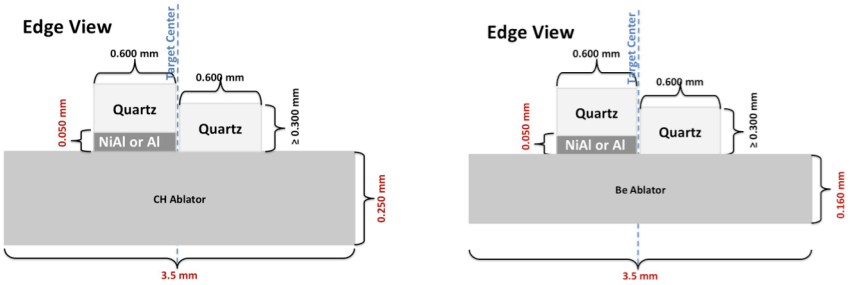

Fig. 1: Illustration of January 2016 MixEOS-EP targets. Targets used either plastic (CH) ablators or beryllium ablators with test specimens of Al or NiAl on top. Quartz witness plates were used to observe transmitted shock steadiness and strength. Primary diagnostic (ASBO line VISAR system) viewed from top.

Prior to conducting the experiments we performed an uncertainty analysis with the expected temporal and spatial uncertainties giving us an idea of the anticipated shock velocity errors of the VISAR measurement. These uncertainties included the inherent temporal resolution of the VISAR interferometer (etalon delay time), streak camera impulse response, and uncertainty in test specimen thickness. These inputs were used to generate shock speed uncertainty curves for the side-by-side targets shown above as a function of specimen thickness using the relationship

$$\sigma_v^2 = \sigma_{\Delta x}^2 \left(\frac{1}{\Delta t}\right)^2 + \sigma_{\Delta t}^2 \left(\frac{\Delta x}{\Delta t^2}\right)^2 \quad (1)$$

where

$$\sigma_{\Delta t}^2 = \sigma_{tb}^2 + \sigma_{etal}^2 \quad (2)$$

and Δx is the specimen thickness, *tb* is timebase of streak camera, *etal* is etalon time delay. This equation is used to generate the curves shown in Fig. 2.

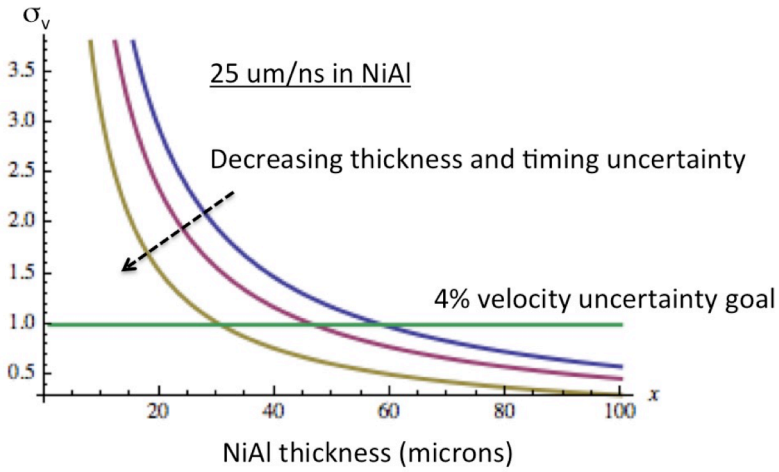

Fig. 2: Expected shock velocity uncertainty curves based on shock transit time through NiAl specimens at 25 μm/ns shock velocity of varying thickness using Eqn 1). The top (purple) curve assumes 60 ps timing uncertainty and 1000 nm thickness uncertainty whereas the bottom (yellow) curve assumes 20 ps timing uncertainty and 500 nm thickness uncertainty.

These curves assumed a 25 μm/ns shock speed in NiAl, but are general over a wide range of velocities. The top curve (purple) with the largest velocity error assumed that specimen thickness was known to 1 μm and the total timing uncertainty was 60 ps. The middle curve assumed the timing uncertainty was 20 ps and the bottom curve assumed target thickness uncertainty was 0.5 μm. Our preliminary estimation of the relative velocity uncertainty required to differentiate between Dalton and Amagat rules was 4%. Figure 2 shows the corresponding specimen thickness required to achieve 4% depending on the actual thickness and timing uncertainty. To achieve these velocity uncertainties we are also constrained to produce steady shocks where pressure and shock velocity remain constant as the shock is traversing the specimen. This sets a constraint on the total specimen thickness based on the laser pulse duration.

In the pressure regime above a few Mbar, the fluid velocity is about 75% of the shock velocity in normal matter. This creates a somewhat slow separation between the shock front and the ablation front in laser driven experiments since the ablation front moves basically at the fluid velocity if viewed in the lab-frame. The maximum steady shock duration one can then realize is about 25% of the laser pulse duration. This max steady shock duration is achieved by setting the ablator thickness equal to the shock transit distance during the full time the laser pulse is on (i.e., laser switches off as shock front reaches ablator/specimen interface). The specimen thickness is then constrained to be equal to (or less than) the shock transit distance for the 25% of laser pulse duration. On OMEGA-EP the maximum laser pulse duration is 10 ns giving a maximum steady shock duration of roughly 2.5 ns. Assuming a 25 μm/ns shock velocity, the maximum specimen thickness is then about 60 μm.

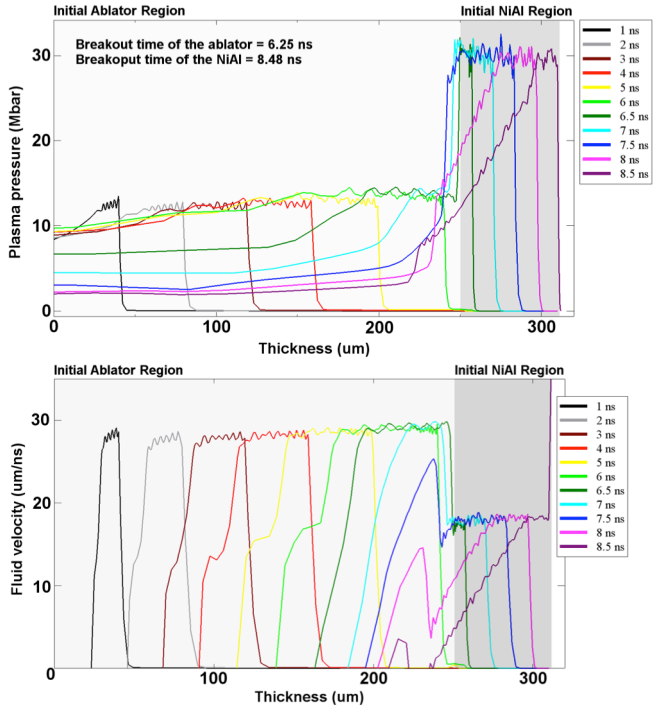

Fig. 3: Preshot design calculations from Helios. The first 250 μm represents the initial position of the plastic ablator and the last 60 μm represents the NiAl specimen. A 6 ns pulse with ~100 ps rise time ramping up to peak power was used with expected OMEGA-EP spot size and energy. The top (bottom) graph shows pressure (fluid velocity) curves at different times while the shock is inside the ablator (t < 6.25 ns) and while the shock is inside the specimen (t > 6.25 ns). The predicted pressure was 30 Mbar, which remained steady inside the specimen.

Design calculations were performed with 1D Helios using OMEGA-EP pulse shapes that were 4 and 6 ns long. With expected full OMEGA-EP energy performance using 2 overlapping laser beams we found that we could achieve approximately 30 Mbar steady shock pressures in our test specimens (see Fig. 3). We used 1.1 mm phase

plates to keep a large illuminated area one-dimensional while still maintaining high pressure. Pulse durations of 4 and 6 ns were also needed to keep high laser power and thus shock pressure as well. For the simulations we used standard SESAME EOS tables for the ablators, quartz, and Al. Since a SESAME table does not exist for NiAl we used the SESAME table for V as a surrogate. From previous experiments and theory (Swift and Loomis, private communication) we know what the shock Hugoniot is for NiAl, which turns out to be nearly identical to V. NiAl and V, not surprisingly, also have very similar initial densities (about 6 g/cc). It turns out this surrogacy was sufficient to set experimental diagnostic timings and VISAR fringe sensitivities.

For each of these pulse shapes we used a different ablator material and thickness (shock transit and laser pulse time still matched) to achieve different shock pressures to have two different mixture rule data points. Beryllium ablators 160 μm thick were used with the 4 ns pulse and CH ablators 250 μm thick were used with the 6 ns pulse. Al and NiAl test specimens were all 50 μm thick to ease target fabrication.

Experimental details of shots in January 2016

The four long-pulse beams were split up into two pairs (Beams 1&3, 2&4) to increase the shot rate. Only 3 large (1.1 mm) DPP were available, so Beam 2 used an 800 um DPP because it has the lower energy performance out of the Beam 2&4 pair. To decrease the effects of using a smaller DPP on only one beam, we used a fire-polishing technique where the aberrant beam was delayed slightly relative to the larger beam. This technique assumes the first beam to hit the target sets the seeds for the shock front, and that delaying the second beam results in the second beam primarily adding energy to the system but not affecting the shock front shape. The following table summarizes the laser pulse settings used on our January 2016 shot day.

Purpose	Beams	Pulse	Energy (UV)	Start Time	DPP
SbyS-CH	1,3	ERM6002v001 (6 ns ramp)	3100 J/ 3500 J	0 ns	wEP-SG8-1100
SbyS-Be	2,4	ERM4002V001 (4 ns ramp)	1750 J/ 2750 J	0.15 ns/ 0 ns	wEP-SG8-0800/ wEP-SG8-1100

Table 1: Pulse shape parameters used on shot day for the Side-by-Side-CH and –Be ablator targets.

Example as-shot laser power histories for both the 4 and 6 ns pulse shapes are shown in Fig. 4. Here we show the individual beam pulse shapes and their total when overlapped on target. Due to the maximum available energy for each beam, the two total laser powers at their peak reach 1.4 TW so the intensity on target for each target type was about the same. Differences in shock pressure then only came

from ablator material efficiency and impedance match differences at the ablator/specimen interface. Time-dependent power variations were observed in the pulse shapes, which showed up as slight shock velocity variations in our ASBO data.

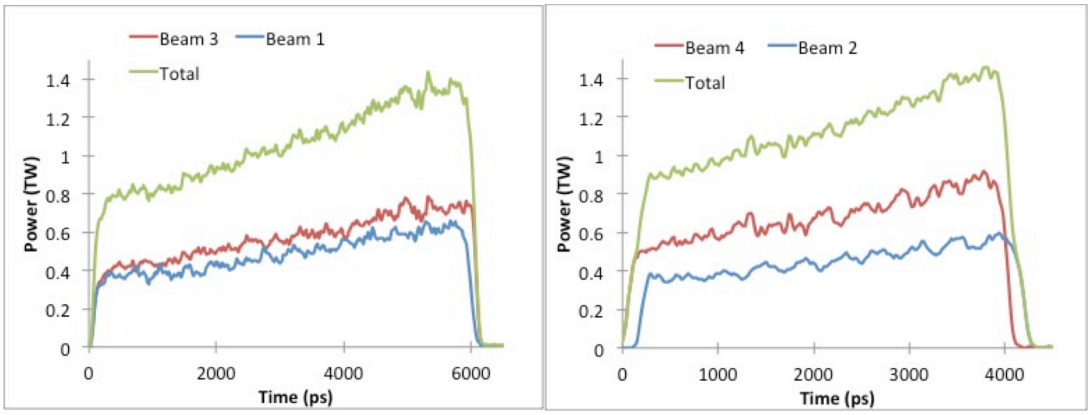

Fig. 4: As-shot ERM6002v001 and ERM4002V001 pulse shapes used in MixEOS-EP.

Our primary diagnostic was Active Shock BreakOut or ASBO, which is a velocity interferometry system for any reflector (VISAR) system. The ASBO has two separate interferometry arms tied to two fast streak cameras. The settings for the two ASBO legs are shown in Table 2.

	Leg 1	**Leg 2**
Interferometer	1A	2A
Etalons	2A (21 km/s/f) 10.8 ps delay	5B (8.75 km/s/f) 25.9 ps delay
Sweep Speed	3/9 ns	5/15 ns
Center of Sweep	Variable 5 ns (SbyS-Be) or 7 ns (SbyS-CH)	Variable 5 ns (SbyS-Be) or 7 ns (SbyS-CH)
Fiducial Delay	3.06 ns (SbyS-Be) 5.08 (SbyS-CH)	3.05 ns (SbyS-Be) 5.10 ns (SbyS-CH)

Table 2: ASBO diagnostic parameters used on January 2016 MixEOS-EP shot day. Leg 2 had a greater velocity sensitivity but poorer temporal resolution compared to leg 1.

On the shot day we started at the slower sweep speed on each leg (9 and 15 ns) until timing was confirmed. We then switched to the fast sweeps to improve streak camera temporal resolution. Streak camera timing was set so that we would observe the breakout time of the ablator (quartz side) as well as breakout of the specimen in each interferometry leg. Due to differences in ablator thickness these

event times changed on alternating shots so we changed streak camera timing along with each target type.

The summary of target types used is shown in Table 3.

Target ID	Color Code	Main Target Description
SideBySide-NiAl	1-4 Red	**Target with 250 µm CH ablator w/ 3 um Gold coating. Test material is NiAl with height of 50 µm and quartz.**
SideBySide-Al	1-2 Blue	**Target with 250 µm CH ablator w/ 3 um Gold coating. Test material is Al with height of 50 µm and quartz.**
CHdrive	1-2 Purple	Drive characterization and timing target with bare **250 µm CH ablator and quartz covering half (NO Au or NiAl)**
SideBySide-Be-Al	1-4 White	**Target with 160 µm Be ablator w/ 3 um Gold coating. Test material is Al with height of 50 µm and quartz.**
SideBySide-Be-NiAl	1-4 Gold	**Target with 160 µm Be ablator w/ 3 um Gold coating. Test material is NiAl with height of 50 µm and quartz.**

Table 3: Target request summary for January 2016 MixEOS-EP shot day

For this shot day we had targets with Al and NiAl specimens for each ablator CH and beryllium. All targets had a piece of single crystal quartz witness plate next to the specimen and on top of the specimen to observe the shock velocity steadiness and strength. These targets also had 3 µm thick Au preheat shields whose thickness was chosen based on preshot simulations with multigroup radiation transport. Two targets were also available that had neither a test specimen nor Au preheat shield. This target's purpose was to directly observe the shock inside the ablator to measure steadiness and shock strength.

Since we are testing EOS mixing rules in these experiments it is important that we know well the atomic constituency of our test specimen. Between 45 and 60 at.-% Ni, the Ni-Al alloy system forms the intermetallic compound NiAl, which has two interpenetrating cubic crystal lattices whose sites are occupied by the Ni and Al atoms [1]. In this crystal phase it also has a well-known density vs. Ni concentration relationship where the density rises linearly from 6 to 6.5 g/cc between the Ni concentration of 50 to 60 at.-%. MST-7 measured our Ni-Al specimen density to be 5.38 g/cc. According to the Noebe et al. [1] relationship this would put our Ni concentration at 45.6 at.-%. However, MST-7 also measured the specimen concentration directly following the experiments. The measured constituency was 61.2 at.-% Ni, 37.8 at.-% Al, and 1 at.-% Mn. At this high Ni concentration (along with the small amount of Mn) it is likely that our specimens were of the Ni_3Al phase,

which we assume does not exactly follow the NiAl phase density relationship. In our simulations below we have used the measured concentration and density.

As Eqn. (1) shows, the measurement shock velocity uncertainty depends on the specimen thickness and thickness uncertainty. Our original plan for determining specimen layer thicknesses for each target was to perform high-resolution (10 nm height deviation) surface scans of the individual target components (prior to assembly) and finished target. The target fabrication team performed the scans using ZYGO white-light interferometer. Each piece of test material, Al or NiAl, was scanned before assembly to get a baseline thickness profile of the piece. Then the entire target was scanned after the material piece was glue to the ablator. The surface scans did not include the quartz witness pieces, since they are transparent to visible light and cannot be diagnosed with the ZYGO. A sample target and ZYGO scan are shown in Figure 5.

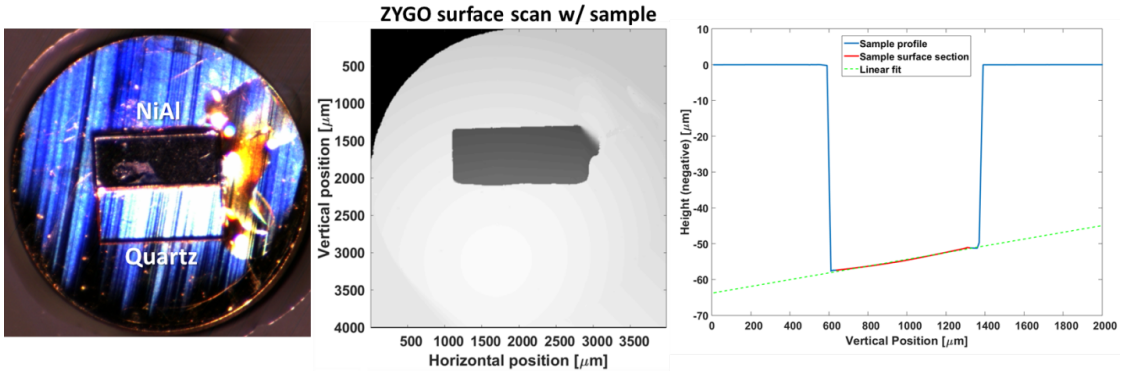

Figure5: (left) Sample target picture. (center) High-resolution ZYGO target scan showing the NiAl sample. (right) Vertical line-out across the NiAl sample after removal of the linear background due to target tilt on the mount. Includes a linear fit to the sample surface to characterize sample thickness variation.

We used a comparison of the before and after assembly scans in order to get an estimate of the glue layer thickness, because the sample height from the ablator surface is the glue layer thickness plus the original sample thickness. Since the scans measure the entire surface profile, this comparison can tell us about the flatness of the glue layer and give us an estimate of the layer thickness variation for inclusion in our error analysis. Similarly, the full scans can tell us both the height of the sample in the diagnostic field of view (FOV), as well as the surface height deviation. We used the maximum slope of linear fits to the pre-assembly sample surface to bound the surface height deviation over the number of VISAR fringes used to determine the shock breakout time from the material. As we discuss later, this procedure proved to be unreliable, primarily because the individual part scans were affected by a (potentially) uneven reference surface as well as micron-sized burrs on the specimen edges. We discuss these issues and their consequences on data analysis more below.

Shot day measurements and data analysis

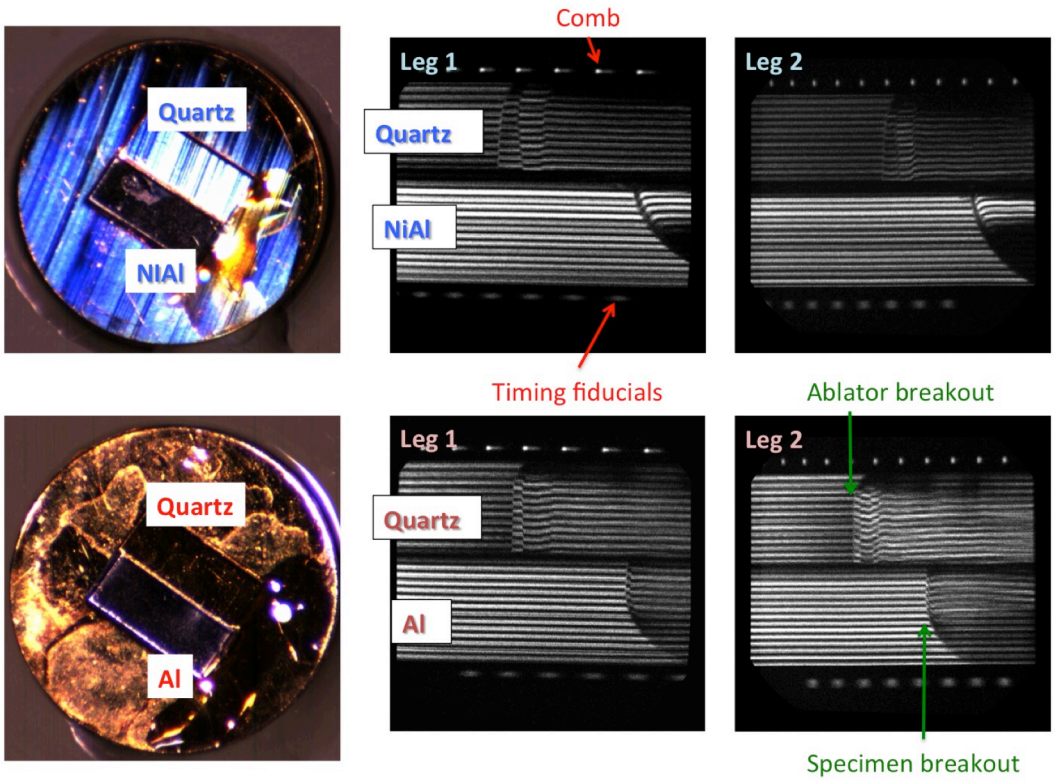

Fig. 6: Example target photos and raw ASBO data from MixEOS-EP. For each ASBO leg we had a comb pulse used for determining time base and fiducial pulses that set absolute timing relative to t_0. Fringe motion in the top half of each streak camera record (time going to the right) is due to a shock propagating through quartz. In the lower half is observed shock breakout of the test specimen and subsequent fringe motion from propagation inside another quartz witness.

In Fig. 6 we show the as-built target and raw ASBO streak camera data for a CH ablator/NiAl target (EP shot 22586) and a beryllium ablator/Al target (EP shot 22587). The ASBO viewed at the center of the target across the quartz/specimen interface extending about 400 μm on either side. In these data we observed the time at which the shock front broke out of the ablator and entered the quartz witness, the subsequent shock velocity history in the quartz witness, the time the shock broke out of the specimen, and the subsequent shock velocity in the quartz after leaving the specimen. Unexpectedly, we also observed secondary shock features (fringe jumps) shortly after breakout from the ablator into the quartz witness. These additional features come from shock reverberations inside the Au preheat and glue layers used in mounting the target pieces, which we do account for in post-shot simulations.

Analysis was carried out via a Fast-Fourier Transform method illustrated in Fig. 7. The specific analysis steps are provided in this figure as well. The important results

from this analysis is the determination of relative time between shock events through the streak camera time base by a 4th order polynomial fit to the diagnostic comb pulses and the retrieval of a velocity map as a function of position and time from each ASBO leg on each shot. From the 4th order polynomial fit procedure we also determined the error associated with each fit parameter, which, when combined, gives the total time base uncertainty between two events as

$$\sigma_{tb}^2 = \sigma_{k1}^2 (n_x)^2 + \sigma_{k2}^2 (n_x^2)^2 \qquad 3)$$

where k1 and k2 are parameters from the fit and n_x is the number of pixels between events of interest in the streak camera record.

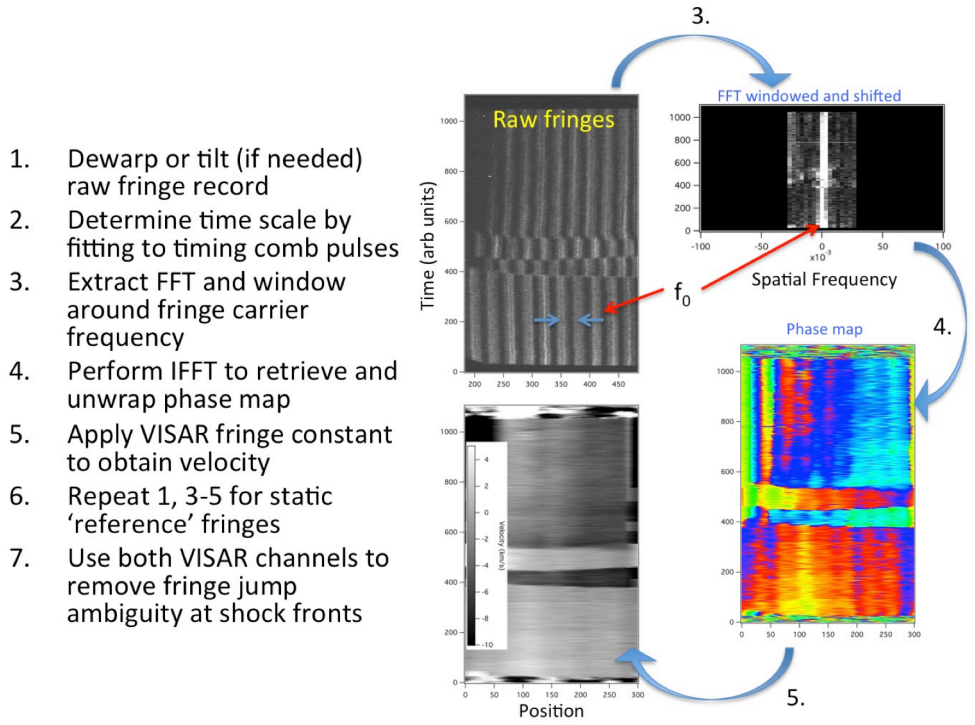

Fig. 7: Illustration of analysis procedure used to extract spatial and temporal velocity maps from ASBO fringe data. Actual analysis steps are described to the right.

The velocity map retrieved through the FFT procedure for a single VISAR leg is ambiguous if there are discontinuous fringe jumps present in the data. Both legs must be analyzed together in order to remove those ambiguities by adding/removing integer fringe jumps until the resulting velocities match. This is made possible only if the fringe constants (velocity per fringe) of each leg was chosen such that they themselves are not integer multiples of each other.

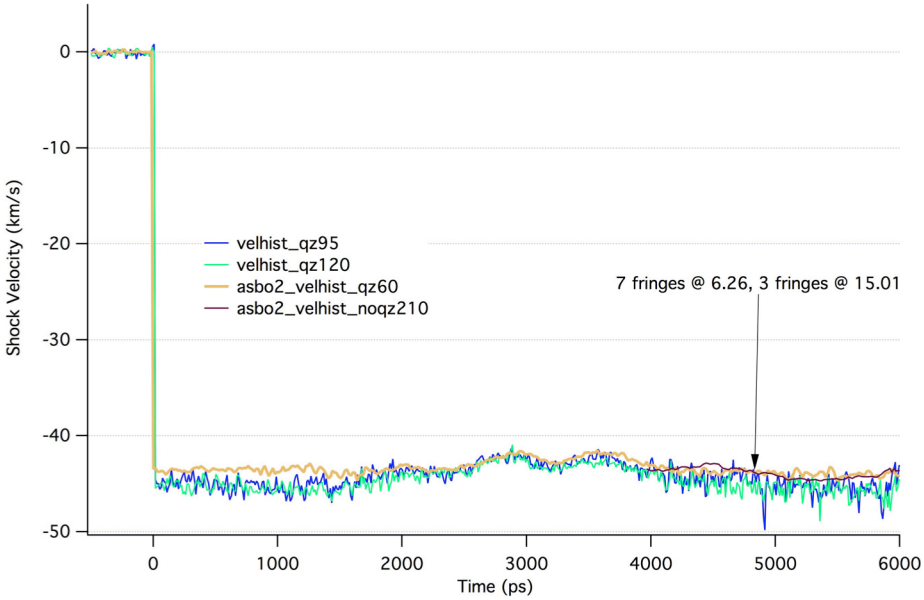

Fig. 8: Analyzed shock velocity history inside a plastic ablator (shot 22582). The various curves are from each interferometry leg showing agreement in achieved ablator shock velocity.

Figure 8 shows shock velocity measurements inside the plastic ablator (shot 22582), which was enabled by removing the Au preheat layer and specimen. The two ASBO legs gave agreement on velocity by adding 7 fringe jumps to leg 2 and 3 fringe jumps to leg 1. For this analysis we used the index of refraction for plastic to recover the true velocity per fringe since there is an apparent velocity correction while a shock is traveling through a transparent medium. The ablator average shock velocity was measured to be about 42 μm/ns. Some undulations in the velocity history were observed, which as simulations support, comes from time dependent power variations in the laser pulse. For this shot we also provide the time base fit parameters and uncertainties (see Table 4) as well as the uncertainty in measured shock velocity. (see Table 5) It is common to assume the fringe unfolding routine is sensitive to 1/10 of a fringe shift, which gives an estimate of the velocity uncertainty for the fringe analysis. This value (+/- 0.6 μm/ns for leg 2) is provided in Table 5.

parameter	value	Error +/-
K0	-1742.7 ps	19.9 ps
K1	12.646	0.142
K2	-0.003625	0.000295
K3	1.7E-6	1E-7
Δt_{abl}	5900	120 ps
Ablat. thickness	245 μm	
Shock f/B.O.	-41.5 μm/ns	

Table 4: Parameters and uncertainties extracted from time base fit for shot 22582. The final row gives measured shock velocity inside the ablator using shock transit time.

	Velocity per fringe	Shock at B.O.	1/10 fringe uncert.
Leg 1	15.01 μm/ns/f	-45.5 μm/ns	1.5 μm/ns
Leg 2	6.26 μm/ns/f	-44 μm/ns	0.6 μm/ns

Table 5: Measured values of ablator shock velocity (shot 22582) using fringe unfolding routine along with the 1/10 fringe uncertainty.

Figure 9 shows analyzed shock velocity data inside quartz for a plastic ablator and Al specimen target (shot 22588). We see that the shock exited the Au preheat shield and entered the quartz at 6.185 ns. The green curve is a lineout from the raw data on the Al side showing shock breakout of the Al at 7.661 ns (where signal increases). The specimen (+ glue) thickness was 53.7 μm giving an (average) shock speed inside the Al (and thin glue layer) of 35.85 μm/ns based on the transit time.

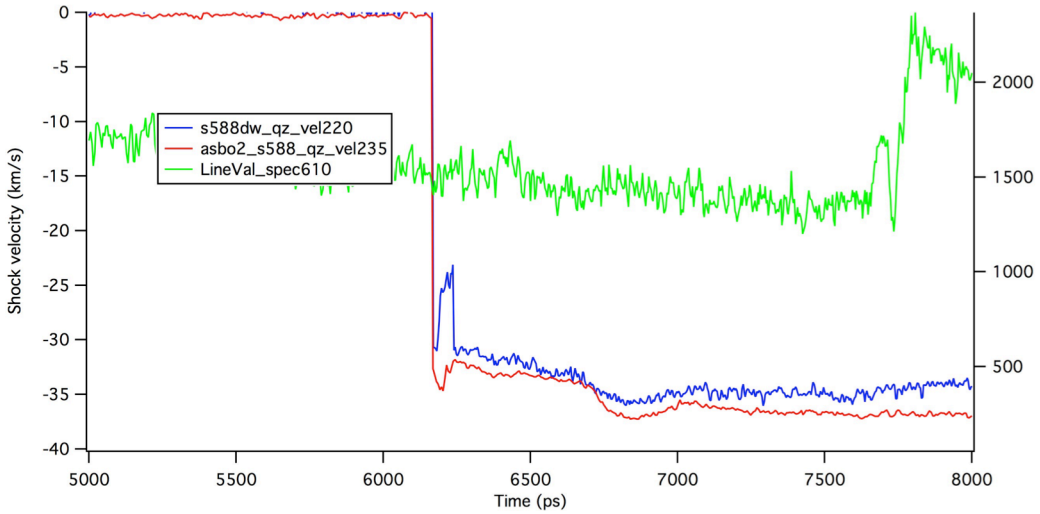

Fig. 9: Shock velocity measurements from a CH ablator/Al specimen target (shot 22588). The red and blue curves show the shock velocity inside the quartz witness following breakout of the ablator as measured by each Leg 2 and Leg 1, respectively. Green curve shows signal level corresponding to shock breakout of the Al, which we used to set shock transit time through the Al.

Data from a streaked optical pyrometer (SOP) was also taken on each shot. Its purpose was primarily as backup if ASBO problems were encountered.

Description of post-shot RAGE simulations and data comparisons

A. The RAGE Code

An adaptive mesh refinement (AMR) Eulerian code called RAGE [2] was used to simulate the experiments in one dimension (1-D). An Eulerian code follows fluid motion through a fixed grid [3], while the AMR allows the mesh to be refined in regions where shocks, sheared flows, or other rapid changes in fluid properties need to be resolved in more detail. We used the recently added laser package to model the absorbed laser energy in the ablator and the resultant shock generation. The source is 1-D and did not include any laser beam speckle imprinting or other illumination irregularities. We find that the absorbed energy is about 2.4 kJ for the 6 ns pulse, which is about 36% of the incident laser energy. This was similar to what was found for other experiments, such as shock/shear. The initial mesh typically consists of the CH (or Be) ablator, the gold and glue layers, the Al or Ni/Al sample (if present), the quartz cap, and an outer low-density "vacuum" region to accommodate material expansion. The target materials had initial zones as small as 0.25 μm, although the cells can be up to 0.5 μm wide in the middle of a material. The

surrounding "vacuum" cells can be up to 1 μm wide. During shock propagation, the code refined the zoning to capture the shocks as they pass through the target. Computer generated opacity mixtures from the TOPS database [4] and Sesame equation of state [5] tables are used. We used the EOS option in the TOPS code to generate Ni/Al tables for the different mixing rules, as well as using the Amagat Law method within RAGE itself.

We ran simulations using the as-shot pulse from the Omega shot library. The targets were set up in 1-D planar mode with the laser beams coming in from the right, as shown in Fig. 10.

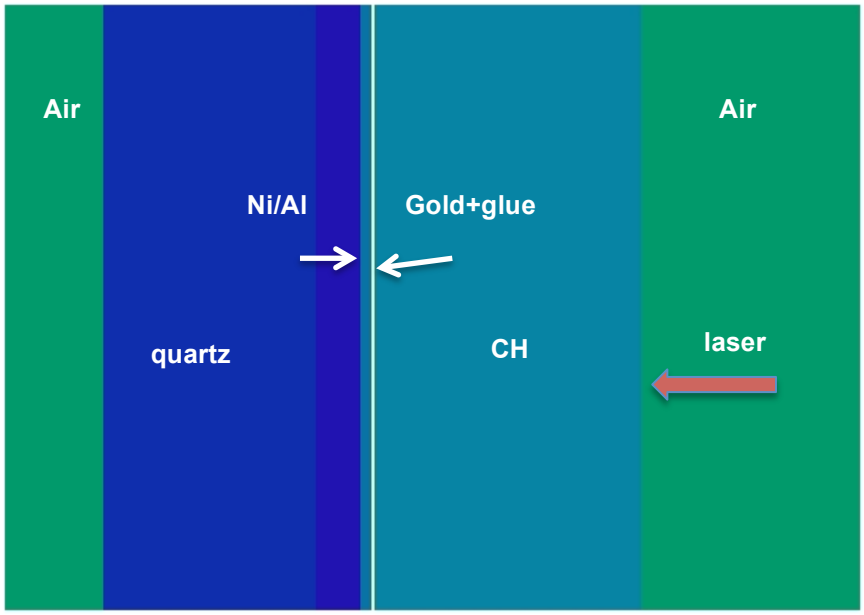

Fig. 10 Density plot of an Ni/Al target. Green is the background "air", the light blue CH ablator is on the right, the dark blue is quartz, white is the gold and glue, and the small region between the quartz and gold+glue is the Ni-Al target sample. The laser rays come in from the right.

B. Simulation results

We started our simulations with the simplest target type, which was a CH slab overlain by gold. This enabled us to determine that we were modeling the laser absorption and resultant shock through the CH ablator correctly. We modeled shot 22582, which consisted of a 245 μm thick CH ablator overlain by gold and quartz. We obtained a value of 41.5 μm/ns for the shock velocity (significantly higher than the 31.1 μm/ns fluid velocity, see Fig. 11). (The "choppy CH shock velocity arises from numerical differencing.) The shock breaks out of the CH at 5.90 ns in the simulation compared to 5.90 ns in the data (with a measured shock velocity of 41.5 μm/ns).

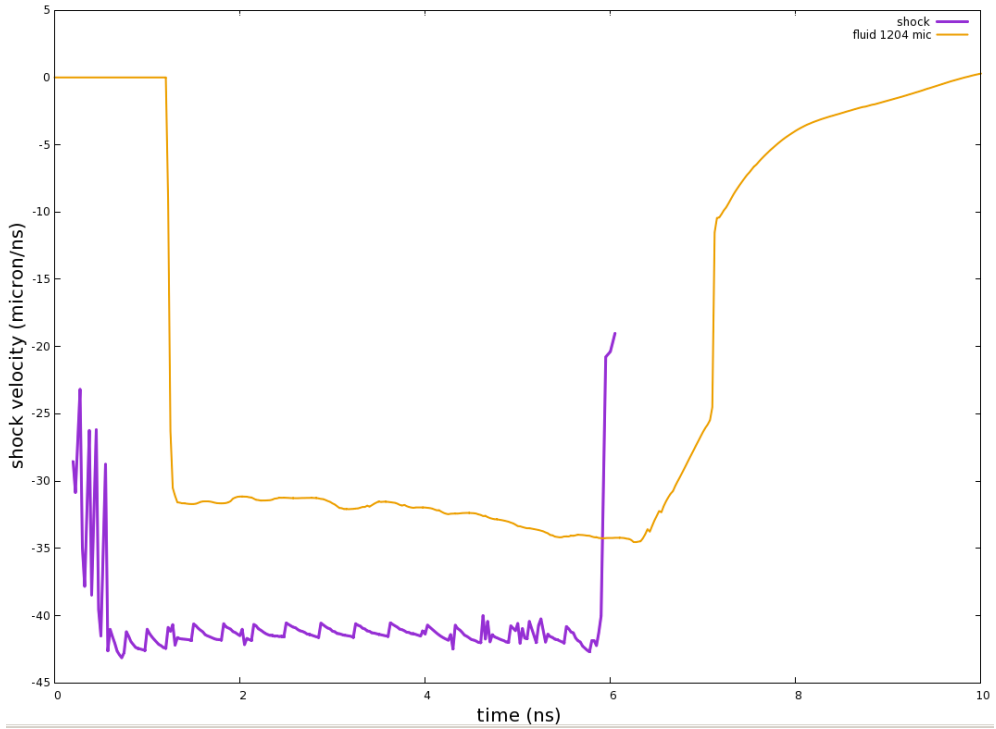

Fig. 11: Shock velocity (purple line) through the CH/Au target of shot 22582 compared to the fluid velocity (gold line). The shock velocity in the CH is about 41.2 μm/ns while the fluid velocity is only 31.1 μm/ns. The shock breakout time is 5.90 ns, the same as the experimental 5.90 ns.

Buoyed by this encouraging result, we then proceeded to model shot 22588, which had a 250 μm thick CH ablator (sesame 7590) overlain by 3 μm of gold (sesame 2700), with a 53.7 μm layer of glue (sesame 7603) and Al on top. The Al was in turn overlain by a 200 μm thick quartz "window" (sesame 7381). Although not explicitly measured, we believe the glue layer is about 2 μm thick. The Al has a well-tested EOS (sesame 3720) and there are no mixing issues. Our average shock velocity in the CH was 41.4 μm/ns, consistent with the previous shot and the shock breakout time was 6.175 ns. This compares well with the experimental time of 6.17 ns (see Fig. 12). We also had an experimental shock breakout time of 7.66 ns for the Al. Our simulation had a shock breakout time of 7.70 ns, which was 34 ps greater than the experimental value (see Fig. 12). This difference was the same size as the breakout time measurement uncertainty of 52 ps. The measured Al+glue shock speed was 35.8 μm/ns, compared to the simulation value of 35.2 μm/ns. We consider the comparison to be satisfactory, given that the simulation results lie within the measurement errors.

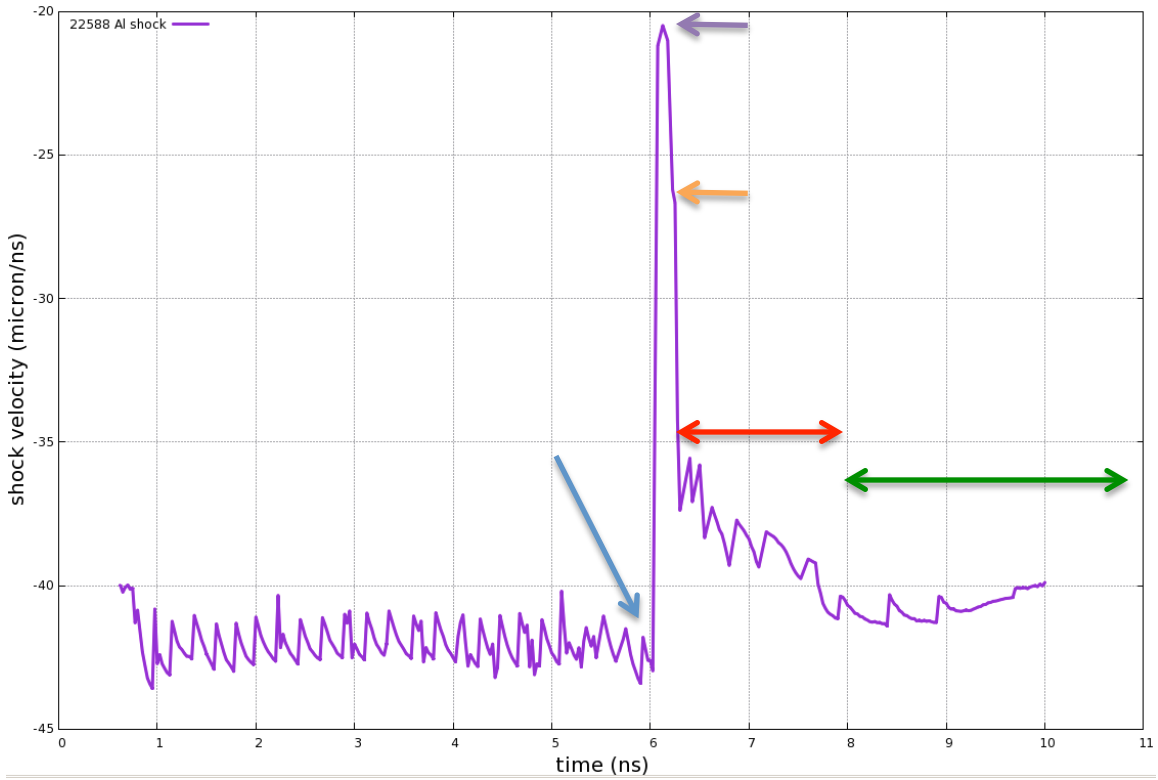

Fig. 12: Shock velocity (purple line) through the CH/Au/glue/Al/quartz target of shot 22588. The shock velocity in the CH was about 41.4 μm/ns. The shock breakout time from the CH was 6.175 ns (blue arrow), compared to the experimental 6.17 ns. The shock was in the gold (purple arrow), glue (orange arrow), aluminum sample (red arrow; 37.3 μm/ns). Finally the shock breaks out into the quartz (green arrow).

We then turn to our final test of the Ni/Al sample, which was shot 22586. We use sesame [5] tables 3720 for Al and 3101 for Ni. This shot had a 250 μm thick CH ablator overlain by 3 μm of gold, and a 52.6 μm layer of glue and Ni/Al on top. The Ni/Al was in turn overlain by a 200 μm thick quartz "window". Although not measured explicitly, we believe the glue thickness is about 2 μm. The experiment produced breakout times of 6.3 and 8.0 ns for the CH and Ni/Al respectively. These were both slightly later than the values for the Al target shot 22588. Our additive volume simulation (see Fig. 13) gave breakout times of 6.275 and 8.025 ns (Δt = 1.75 ns), compared to the experimental values of 6.32 and 8.02 ns (Δt = 1.70 ns). The CH simulated shock velocity was 41.6 μm/ns (see Fig. 13), which was faster than the 39.7 μm/ns of the experiment. The simulated Ni/Al+glue shock velocity was 28.8 to 30.1 μm/ns (depending on the mixing rule), which was similar to the 30.9 μm/ns of the experiment. We also ran the same shot using the ideal gas additive volume, partial pressure (Dalton), and Rage Amagat mixing rules. (See Abdallah [6] for detailed descriptions of the difference in these mixing rules.) The partial pressure gas rule had the slowest shock breakout time of 8.100 ns, while the other three mixing rules had the same breakout time of 8.025 ns, which is only 75 ps earlier (see Figure 14). We provide a summary of the measured and simulated shock

breakout times in Table 6. (The shock transit time for 2 μm of glue is 75 ps in all the simulations. These breakout time differences from the different mixing rules were close enough to be slightly more than the measurement error described earlier.

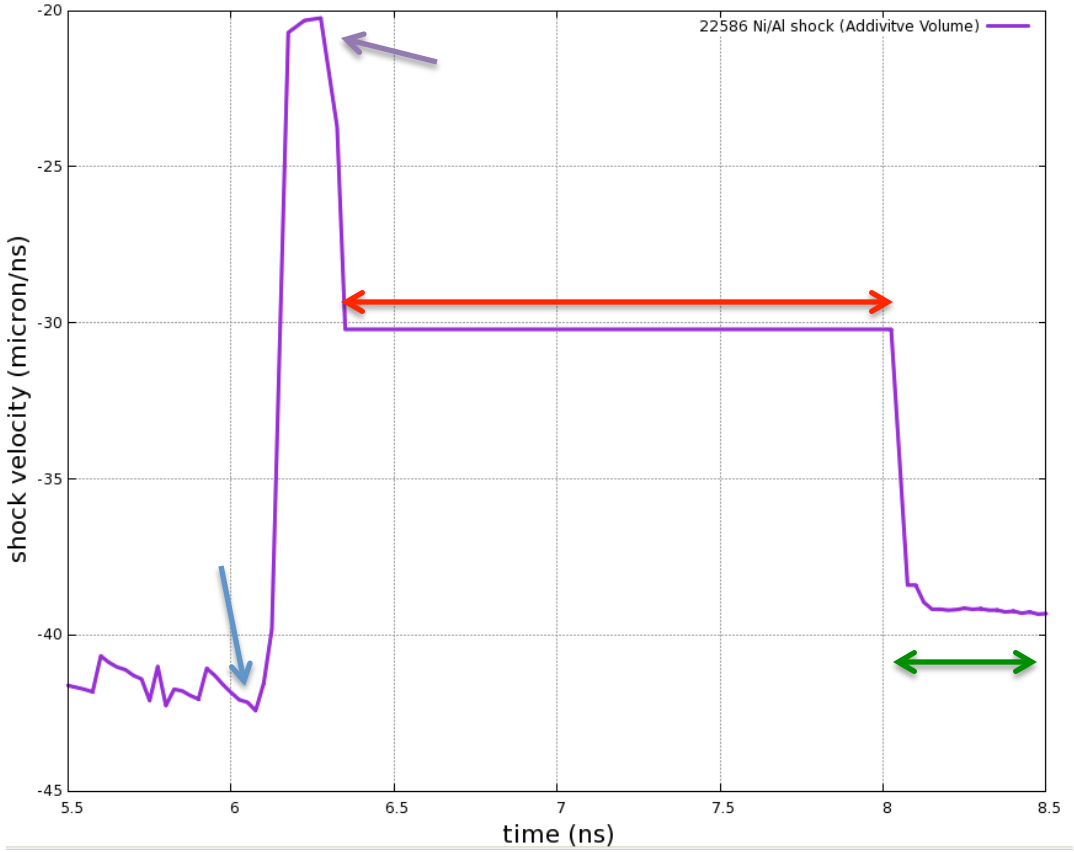

Fig. 13: Shock velocity (purple line) through the CH/Au/glue/NiAl/quartz target of shot 22586. The shock velocity in the CH was about 41.6 μm/ns. The shock breakout time from the CH was 6.275 ns (arrowed), compared to the experimental 6.32 ns. The shock velocity in the Ni/Al sample was between 28.8 and 30.1 μm/ns (red line), depending on the mixing rule used. The speed of the shock in the gold was 24 μm/ns (purple arrow) and in the glue was 30 μm/ns.

Our not being able to measure the thickness of the glue layer explicitly concerned us enough that we ran simulations with glue thicknesses between 1 and 4 μm for our simulations of shot 22588 and 22586. Although the timing of shock breakout from the glue into the Al (or NiAl) sample changed, the time of shock breakout from the sample into the quartz was unaffected. We were not surprised with this result for the NiAl simulations, because the shock velocity of the glue and NiAl are almost the same. For the Al sample, changing the glue thickness from 1 to 4 μm caused the shock breakout time of the glue+Al sample to vary by 25 ps. The transit time through the glue varied from 25 ps (1 μm) to 125 ps (4 μm). We also examined the effect of increasing the laser power by 2% and found the breakout times were 50 ps earlier, while the transit time stayed the same at 1.525 ns. The

shift of 25 ps results in a 0.6 μm/ns change in shock speed. When we changed in the time spacing between tracer particle edits (from 10 to 25 ps) and the resolution of tracer particles (from 1 to 0.5 μm) produced an uncertainty of ±0.4 μm/ns in the simulated shock propagation values. Thus, we estimate that the total uncertainty in our simulated shock speeds is 0.4 μm/ns (NiAl) to 0.7 μm/ns (Al). This is similar to the previously quoted measurement uncertainty of ±0.6 μm/ns.

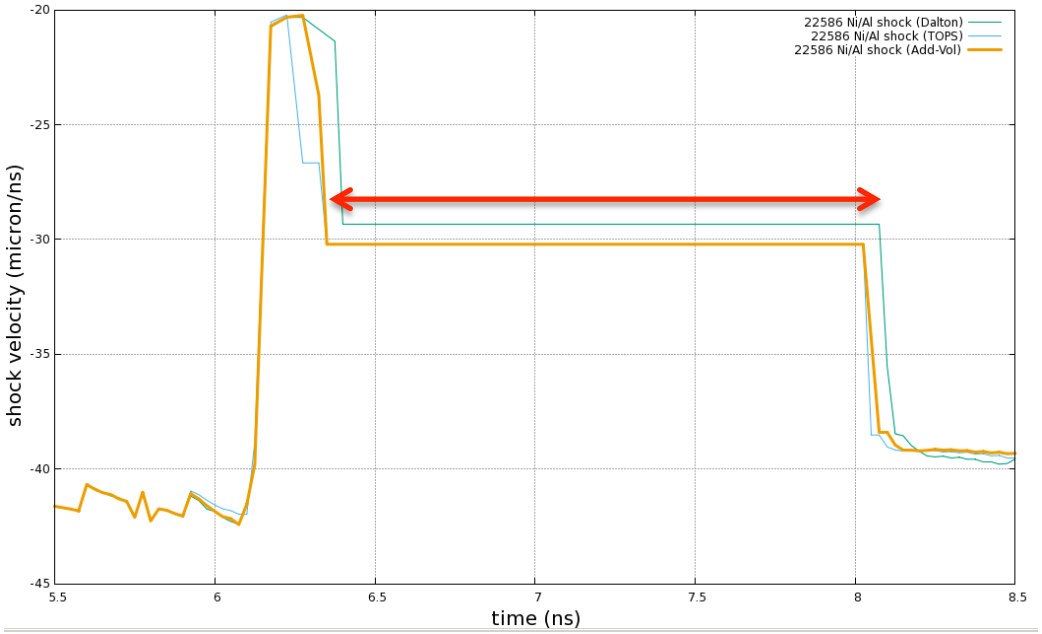

Fig. 14: Shock velocity comparison in the NiAl sample for different mixing rules. The Amagat, ideal gas, and additive volume (gold and blue lines) had a breakout time of 8.025 ns. Green is the Dalton (partial pressure) rule with a breakout time of 8.100 ns. The experimental breakout time was 8.025 ns. The shock in the NiAl is denoted by the red arrow.

Table 6: Summary of breakout and transit times

Shot #	Sample	Ablator + Au breakout time (ns)		Sample+ glue thick (μm)	Sample + glue transit time (ns)	Mix rule	Sample transit time (ns)	shock velocity (μm/ns)	shock velocity (μm/ns)
		Expt	Sim	Expt	Expt		Sim	Sim	Expt
22582	None	5.90	5.900	N.A.		N.A.			
22586	Ni/Al	6.32	6.275	52.61	1.705	Add Vol	1.750	30.06	30.86
22586	Ni/Al	6.32	6.275	52.61	1.705	Part Pres	1.825	28.83	30.86
22586	Ni/Al	6.32	6.275	52.61	1.705	Ideal gas	1.750	30.06	30.86
22586	Ni/Al	6.32	6.275	52.61	1.705	Rage EOS	1.750	30.06	30.86
22588	Al	6.17	6.175	53.70	1.498	sesame Al 3720	1.525	35.21	35.85

Conclusions

In this work we have measured shock velocity in Al and NiAl specimens at 30 Mbar to test EOS mixing rules of metals at high energy density. Experiments were designed to minimize measurement uncertainties in order to differentiate between closely behaving mixing rule models. Steady (less than 1 μm/ns variation) shocks were generated using novel thick ablators where the only unsteadiness came from variations in the laser power history and necessary Au preheat and glue layers. By modeling all layers and the as-shot laser power, simulations were able to closely match shock velocities and transit times in our reference Al specimens. Upon applying the mixture rules we were also able to closely match NiAl behavior.

From the simulation results shown in Table 6 we find that a total shock velocity uncertainty of +/-1.5% was needed to differentiate between the slowest (Partial Pressures) and fastest (all other) mixing rule shock velocities. To differentiate between the Additive Volume and Partial Pressure mixing rules would require a new experiment where specimen thickness (and thus transit time) was substantially increased. Another option would be to use materials with a greater atomic number difference or that otherwise show a larger shock velocity difference for the different mixing rules.

The effect of the thin glue layer used to hold the specimen and quartz pieces onto the ablator turned out to be greater than we anticipated going into the experiment shot day. Even though the glue layers were only a few microns thick, they showed up clearly in our VISAR traces and their thicknesses could not be accurately measured. The ambiguity created by the glue (and Au preheat shield) shock features, along with the likely scenario that the glue was not the same thickness under the quartz relative to under the specimen, meant we could not faithfully identify the time during the VISAR record when the shock entered the specimen. We eventually decided that the only true comparison we could make between data and simulations was the transit time and (average) shock velocity through the combined glue + specimen layers. In our simulations, we found that for glue thicknesses of a few microns, the effect of not knowing the actual glue thickness is small, especially for the NiAl samples. The only reason this level of detailed modeling and analysis was needed was due to the requirement of achieving a 1.5% uncertainty, which we still got close to.

In performing these experiments we learned a number of lessons that we would apply in future experiments. Primarily, for highly accurate EOS measurements of this type a better way of measuring individual and assembled target layers is needed to minimize thickness uncertainties (this includes methods for measuring glue thickness). We also, having now updated our VISAR analysis routines during this data analysis, have a better understanding of how to determine and set streak camera timing uncertainty. We have also learned new methods along these lines following useful discussions with Peter Celliers (LLNL) about remapping streak records to purely linear temporal pixels.

These experiments were a nice test of the new Rage laser package, which performed admirably. Rage also does an excellent job of modeling the shock propagation through these laser driven samples, which is an encouraging extension of modeling shocks through fluids. A VISAR experiment such as this one was really needed for accurate time-dependent validation of that new simulation capability. Probably the most successful aspect towards that validation from these experiments was the observed shock speed variations inside the ablator that arose from laser power variations. These were also observed in the Rage simulations with about the same amplitude and timing using the as-shot pulse. In the future, we would like to run simulations in 2-D with the laser rays to better examine potential sample edge effects.

One issue we grappled with is the issue in Rage of initializing a mixed cell or even normal EOS to standard temperature and pressure at the desired density when starting with a sesame/TOPS EOS table of slightly incorrect density. Grizzly [6] used to have a scaling function, but this code is no longer available. Presently, the only option is to iterate with T-1 to obtain a new EOS table for each mixing method. We also tried an energy offset in Rage, but that function does not work in three-temperature mode, which the laser package requires. Density scaling (matdef25) introduces spurious initial pressure.

In this report we have not presented any detailed results from the beryllium ablator targets and have focused only on the CH ablators instead. We did this because only for the CH ablator do we have direct measurements of the shock speed inside the ablator, which we used to tune drive in the simulations. We cannot do this with the same accuracy for the beryllium ablators. If so desired, we can continue with the beryllium analysis and simulation comparison, which would help to support our mixture rule comparison by giving more shot statistics at a similar shock pressure. Also for beryllium we have a good measure of preheat since we observed the Au layer expansion with the VISAR prior to shock arrival. This preheat probably changed the ablator state into which the shock was sent (by an eV or so), but the Au preheat shield efficiently prevented specimen heating. With beryllium simulations including ablator preheat we could evaluate the effect on the mixture rule results; the ablator starting temperature and shock velocity through that elevated temperature would change the shock state transmitted to the specimen, thus the simulations might be comparing a slightly different shock state in the specimen than occurred in the experiments.

Acknowledgements

We wish to acknowledge conversations with Tim Clark that helped motivate this work. Forrest Doss, Tim Clark, Jacob Stickney, Isaac Ortiz, Rob Gore, and Chris Fontes provided helpful discussions and simulations during this project. We thank C10 and C4 for funding support.

References

1. R.D. Noebe, R.R. Bowman, M.V. Nathal, International Materials Reviews, **38**, 4 (1993).
2. M. Gittings, R. Weaver, M. Clover, T. Betlach, N. Byrne, R. Coker, E. Dendy, R. Hueckstaedt, K. New, W.R. Oakes, D. Ranta, and R. Stefan, Computational Science and Discovery, **1**, 015005 (2008).
3. R.E. Meyer, *Introduction to Mathematical Fluid Dynamics*, (Wiley-Interscience, New York, 1981).
4. See National Technical Information Service Document No. DE06369029 (J. Abdallah, Jr. and R.E.H. Clark, "TOPS, A multigroup opacity code", LANL Rep. LA-10454, 1985). Copies may be ordered from the National Technical Information Service, Springfield, VA 22161.
5. See National Technical Information Service Document No. DE10150216 (J.D. Johnson, "The SESAME Database", LANL Rep. LA-UR-94-1451, 1994). Copies may be ordered from the National Technical Information Service, Springfield, VA 22161.
6. J. Abdallah, Jr., "User's Manual for GRIZZLY", LANL Rep. LA-10244-M, 1984